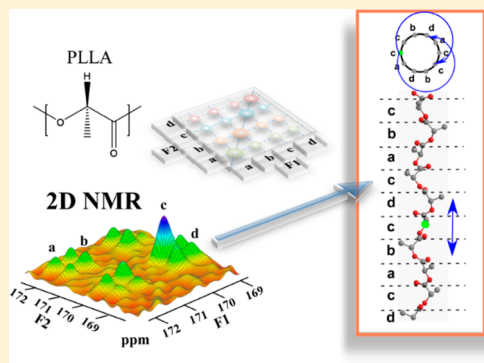


Helical Jump Motions of Poly(L-Lactic Acid) Chains in the α Phase As Revealed by Solid-State NMRWei Chen,[†] Detlef Reichert,[‡] and Toshikazu Miyoshi^{*,†}[†]The University of Akron, Department of Polymer Science, Akron, Ohio 44325-3909, United States[‡]Institut für Physik, Martin-Luther-Universität Halle-Wittenberg, Betty-Heimann-Str. 7, D-06120 Halle (Saale), Germany

ABSTRACT: The molecular dynamics of Poly(L-lactic Acid) (PLLA) chains in the α phase was investigated by Solid-State NMR spectroscopy. ^{13}C high-resolution NMR clearly indicates that the crystalline signals split into 2, 3, and 4 signals for the CH_3 , CH and CO groups, respectively at 25 °C, while the amorphous signals give a broad component at the bottom of the crystalline signals. ^{13}C NMR spectra show that the crystalline line shape changes with increasing temperatures well above the glass transition temperature (T_g) and imply the presence of the molecular dynamics in the crystalline region. Comparisons of the evolution-time dependence of CODEX data and simulation results based on reorientation of chemical shift anisotropy (CSA) indicate that the chains in the α phase perform helical jump motions in the slow dynamic range at temperatures above 115 °C. The mixing-time dependence of the CODEX data yields an activation energy of E_a of (95 ± 8) kJ/mol for the helical jump motions. Moreover, two-dimensional exchange NMR with highly resolved signals for the CO group provides cross peaks among four well resolved signals due to the helical jumps. Comparison of 2D buildup curves of the cross peaks and calculated data determines that helical jump motions prefer largely uncorrelated random back-and-forth motions between the neighboring sites, possibly enabling large-scale chain diffusion in the crystalline regions.



■ INTRODUCTION

The helical jump motion in semicrystalline polymers was proposed by Hoffmann et al.¹ to explain the α_c relaxation in the crystalline region. Since it was first experimentally confirmed in poly(oxyethylene) (POM) crystals via two-dimensional (2D) exchange NMR based on reorientations of chemical shift anisotropy (CSA) in 1987,² it has been demonstrated that various semicrystalline polymers such as polyethylene (PE),³ isotactic-poly(propylene) (iPP),^{4–7} isotactic-poly(4-methyl-1-pentene) (iP4M1P),⁸ isotactic-poly(1-butene) (iPB1) form III,⁹ poly(ethylene oxide) (PEO),¹⁰ etc perform the same type of large amplitude motions in the temperature range above or slightly lower than the glass transition temperature (T_g) but below the melting temperature (T_m). This dynamics includes jump rotations of chains to the neighboring sites around the chain axis as well as translations of the whole chains along the chain axis. Such overall chain dynamics determines mechanical properties such as drawability of semicrystalline polymer materials.¹¹ Also, Schmidt-Rohr and Spiess observed chain diffusions of PE chains between the crystalline and amorphous regions by using 2D exchange and 1D polarization transfer NMR.¹² Recently, several groups investigated morphological effects on chain diffusions and local flip motions of PE.^{13–18} Yao et al. found that chain diffusion is much faster in the single crystals as compared to the bulk crystals and reported that there is a large discrepancy for activation energy (E_a) values between local flip motions and chain diffusions.^{15,17} Bärenwald et al. systematically investigated the molecular dynamics of PE in

reactive powders, nanodisks, and melt-grown crystals^{13,18} and reported similar chain diffusion behaviors in the melt and single crystals. Additionally, the E_a values for chain diffusions of PE determined by Yao et al.^{15,17} and Bärenwald et al.^{13,18} are much smaller than the E_a value determined by Schmidt-Rohr and Spiess.¹²

Long-range chain diffusions are induced by successive local jump motions. Thereby, not only the understanding of the local jump dynamics and chain diffusion but also elucidation of short-range correlations of local jumps are a scientifically and practically important issue in the further understanding of the dynamic nature of crystalline chains as well as the relationship between structure and dynamics. Schmidt-Rohr and Spiess^{10,19} developed 3D exchange NMR methods in which two dynamic windows are inserted in order to stroboscopically observe the degree of coupling of the individual helical jump motions and confirmed the presence of both the return jumps to the original positions and forward jumps to the next positions in the highly orientated POM.¹⁰ This result indicates that individual jump motions decouple from each other and local helical jump motions do not necessarily lead to an efficient directed translation of the crystalline stems between the crystalline and amorphous regions. Even though there are various α_c mobile crystals, research on correlations of individual helical

Received: January 22, 2015

Revised: February 26, 2015

jump motions was limited to the pioneer work on POM due to experimental limitations.

Poly(lactide) (i.e., poly(lactic acid), PLA) is a renewable and biocompatible thermoplastic material with the largest market share of all biodegradable polymeric materials.^{20,21} To make PLA a promising material with properties comparable with those of petroleum-based plastics, an understanding of their microscopic structures and their molecular dynamics in different phases is required.^{22–24} Because of the chirality of the methine carbon, PLA contains two enantiomers: the left-handed poly(L-lactide) (PLLA) and the right-handed poly(D-lactide) (PDLA). The homopolymer of PLA exhibits different crystalline forms, such as α ,²⁵ α' (or δ),²⁶ β ,²⁷ and γ ,²⁸ and can form a stereocomplex (SC) with an enantiomer.²⁹ The most thermally stable α phase (chiral crystal) can be obtained by isothermal crystallization at a temperature higher than 120 °C from the molten state, where two left-handed 10₇ helices (PLLA) are included in the orthorhombic unit cell of $a = 10.68$, $b = 6.17$, and $c = 28.86$ Å with the space group $P12_11$ ³⁰ (Figure 1b). Broad-band dielectric relaxation spectroscopy (DRS)^{31,32}

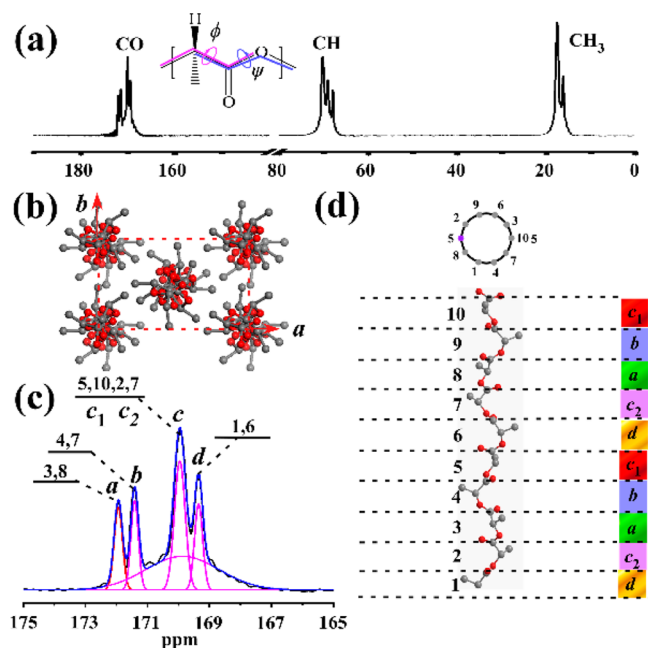


Figure 1. (a) 1D ¹³C CP/MAS spectrum of PLLA in the α phase with a MAS frequency of 6 kHz at 25 °C and (c) its CO region with the peak assignment.⁴⁵ (b) The packing structure of PLLA α phase on the crystallographic ab plane.³⁰ (d) Schematic illustration of the 10 sites in the 10₇ helix.

and solid-state (SS) NMR^{33–36} have been used to characterize the molecular dynamics of PLA in the α phase and the glassy state. Runt et al. investigated the segmental motions of the amorphous regions of the α -rich PLLA and PLLA copolymers³² and found that the segmental motions above T_g are restricted by increasing crystallinity. Similarly, Bras et al. also studied the molecular dynamics of PLLA α -rich samples in a wide frequency and temperature range from 0.1 Hz to 10 MHz and from –100 to 60 °C and 100 to 170 °C, respectively.³¹ They found that the segmental motions of the amorphous chains become faster with increasing crystallinity and did not observe any additional relaxation corresponding to the crystalline relaxation at temperatures well above T_g .²⁸ On the other hand, high-resolution ¹³C NMR line shapes at several

temperatures implied the presence of crystalline chain dynamics with increasing temperature.³³ To reveal the molecular dynamics of PLLA in the crystalline regions, exchange NMR based on reorientation of chemical shift anisotropy (CSA) is definitively necessary.

In this work, centerband-only detection of exchange (CODEX) NMR³⁷ (detecting molecular reorientation by changes of the *anisotropic* chemical shifts) and 2D exchange (based on the exchange between the *isotropic* chemical shifts) are used to investigate the molecular dynamics of the PLLA chains in the α phase in a slow dynamic regime for a correlation time, $\langle\tau_c\rangle$, of 10^{-2} – 10^2 s. The evolution-time dependence of the CODEX decay curve revealed that PLLA chains in the α phase exhibit large-amplitude helical jump motions, similar to those previously observed for several polyolefins^{6–9,38,39} and other polymers.^{40,41} Moreover, the temperature dependence of the $\langle\tau_c\rangle$ values, as determined by mixing-time (t_{mix}) dependence CODEX experiments, shows Arrhenius behaviors with an activation energy of (95 ± 8) kJ/mol. These direct dynamic evidence at molecular levels clearly indicates that PLLA in the α phase is one of the α_c mobile. Besides, 2D isotropic chemical exchange at multiple sites provides detailed correlation between individual helical jump motions. Experimental build-up curves and simulation results prove that individual chains do not perform a directed translation but prefer the random back–forth motion of PLLA in the melt-grown crystals.

EXPERIMENTAL SECTION

2.1. Samples and Preparation Procedures. PLLA with an average molecular weight of $M_w = 700$ kg/mol and a PDI = 1.80 was obtained from Polysciences, Inc. The PLLA sample was first heated to 200 °C and maintained for 5 min, and then was rapidly moved to the hot stage with a preset temperature of 140 °C and was isothermally crystallized for 6 h.

2.2. DSC. DSC experiment was performed using a TA Instruments model Q2000. The samples were heated and cooled at a rate of 10 °C/min. Liquid nitrogen was used to protect the sample and to control the heating or cooling rate. The T_g , T_m , and the crystallinity χ_c were determined by DSC. Using ΔH and reported ΔH_m^0 values of 93 J/g for the α phase,^{42,43} T_m and χ_c were determined to be 185 °C and 51%, respectively. We could not determine the T_g value for the α sample. A glassy sample was prepared through fast quench PLLA melt (annealed at 220 °C for 5 min) into ice water. The T_g value of the glassy sample was 59 °C.

2.3. Solid-State NMR Measurements. All NMR experiments were performed on a Bruker Avance 300 with resonance frequencies of 75.5 and 300.3 MHz for ¹³C and ¹H, respectively. A 4 mm double-resonance probe was used throughout the experiments, and the sample temperature was calibrated using the ²⁰⁷Pb chemical shift of Pb(NO₃)₂.⁴⁴ The ¹³C chemical shift was calibrated externally based on the methine peak of adamantane at 29.46 ppm.

2.3.1. ¹³C CP/MAS. The rf. field strength of the ¹H and ¹³C channels were fixed at 62.5 and 68.5 kHz, respectively. The ¹H–¹³C cross-polarization (CP) contact time and recycle delay (RD) time were 2 ms and 2 s, respectively. ¹H two-phase pulse modulation (TPPM) with a field strength of 62.5 kHz was applied during the ¹³C signal acquisition time of 41 ms. The MAS spinning frequency was set to (6000 ± 3) Hz.

2.3.2. CODEX.^{6,37,40} CODEX experiments detect molecular reorientations of different functional groups in the slow dynamic regime of 10^{-2} – 10^2 s, if the corresponding signals

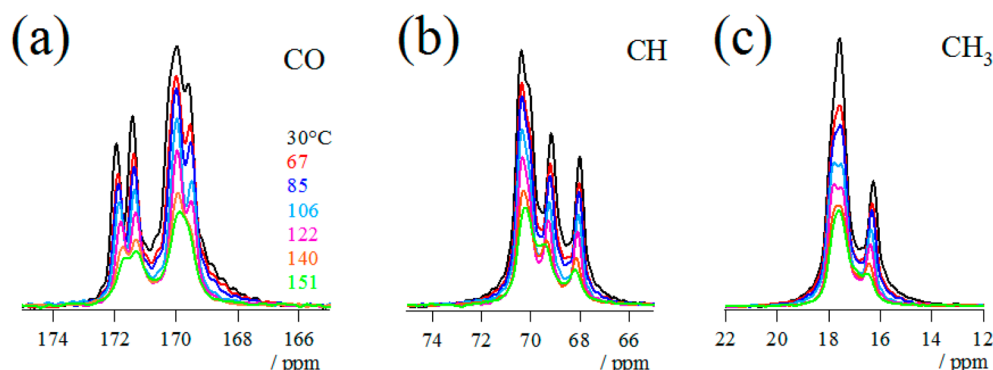


Figure 2. Temperature dependence of ^{13}C CP/MAS spectra of CO (a), CH (b), and CH_3 (c) of the PLLA α -rich sample. Exponential window function with 10 Hz was applied.

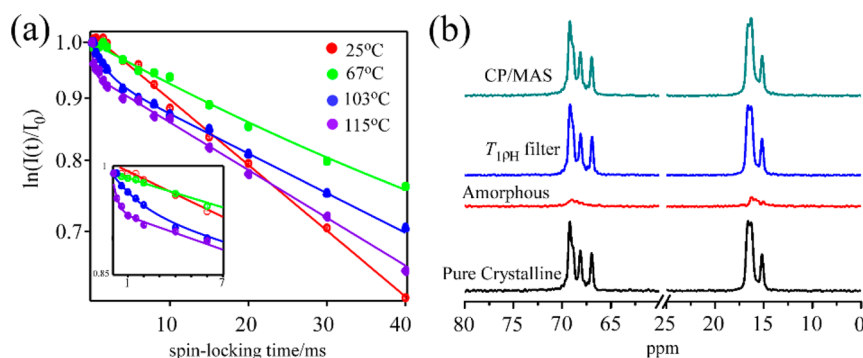


Figure 3. (a) $T_{1\rho\text{H}}$ relaxation behaviors of the PLLA α samples at different temperatures. (b) ^{13}C CPMAS NMR spectra without and with a $T_{1\rho\text{H}}$ filter of 4 ms. Linear combinations of the two NMR spectra produce pure amorphous and crystalline signals.

are highly resolved. A series of rotor-synchronized experiments were performed at a MAS spinning rate of (4000 ± 3) Hz. In the case of the ^{13}C channel, the ^{13}C CSA was recoupled by rotor-synchronized π pulses with a pulse duration of $15.0 \mu\text{s}$ during two evolution periods, which were separated by a mixing time, t_{mix} . When the $\langle\tau_c\rangle$ of the molecular dynamics is much longer than t_{mix} , the magnetization stored in the z -axis after the first evolution will be completely refocused after the second evolution. When $\langle\tau_c\rangle$ is comparable to or shorter than t_{mix} , magnetizations dipphase and the exchange spectrum, S , exhibits signal decay. To compensate for additional decay resulting from relaxations, T_1 and T_2 , and instability of the NMR spectrometer, a reference spectrum S_0 was obtained by switching t_{mix} with the z -filter time, t_z , where t_z was set as one rotor period of MAS. Therefore, the t_{mix} dependence of the normalized signal ratio of (S/S_0) can be used to extract $\langle\tau_c\rangle$. In addition to t_{mix} , another variable parameter is the evolution time, Nt_r , where t_r is the rotation period of MAS and N is an integer. The Nt_r dependence of the CODEX decay curve provides information about the reorientational angle of molecular dynamics.

2.3.3. ^{13}C 2D Exchange. The 2D exchange spectra were acquired by the States-TPPI mode. The number of sampling points was 240 and 128 with a sampling time of $320 \mu\text{s}$ along t_2 and t_1 dimensions, respectively. The other experimental parameters are the same to those used in CODEX.

3. RESULTS

3.1. ^{13}C CPMAS NMR Spectra. Figure 1a shows 1D ^{13}C CP/MAS spectrum of PLLA in the α phase at 25°C . $^{13}\text{CH}_3$, ^{13}CH , and ^{13}CO signals are split into 2, 3, and 4 peaks,

respectively, which result from the discrete chain packing and chain conformations. According to the XRD results, individual stems adopt a 10_7 helical conformation in the orthorhombic unit cell structures. The torsional angles of ϕ (CH–CO) and ψ (CO–O) bonds are 63.0° – 74.2° and 155.9° – 167.6° , respectively.^{30,45} Among three functional groups, the carbonyl group shows the largest splitting number of the peaks with the largest peak separation of 179 Hz. The resolved 4 peaks are labeled by a – d (Figure 1c–d).

Recent DFT calculations by Pawlack et al. assigned these multiple peaks for the CO group to 10 different conformational sites in the 10_7 helix, numbered by 1–10 as follows: $a(3,8)$; $b(4,7)$; $c_1(5,10)$; $c_2(2,7)$; $d(1,6)$ (see Figure 1d),⁴⁵ where c_1 and c_2 overlap with each other and are treated as c . This assignment indicates that 10 sites in the 10_7 helix are repeating by two subunits consisting of 5 monomer units. Additionally, our sample shows a crystallinity of 51% as determined by DSC. The amorphous signals show very broad components due to structural disorders and low mobility below T_g and, thus, contribute to the bottom signal of the sharp crystalline signals. Figure 4c shows the peak deconvolution results supporting the sharp crystalline and broad amorphous components. Actually, there are several techniques to filter out the amorphous signals in the CPMAS NMR spectra. In the following section, we will demonstrate how $T_{1\rho\text{H}}$ can distinguish the amorphous signals from the crystalline signals at several temperatures.

Figure 2 shows ^{13}C CPMAS NMR spectra for all the functional groups of the PLLA α sample at various temperatures above 30°C . The intensities of all the signals decrease with increasing temperatures; however, the line width does not change substantially up to 67°C . The intensity drop is

attributed to the Curie Law.⁴⁶ Some signals begin to merge into one with increasing temperature, for example, the CO doublet signals at 169.3 and 171.2 ppm, CH signals at 70.0 and 69.1 ppm, and CH₃ signals at 15.9 and 17.3 ppm. At 151 °C, these peaks become one resonance line. Other signals also show some chemical shift change with increasing temperatures. These changes imply an increased molecular dynamics of PLLA chains in the crystalline regions.

3.2. Separation of Crystalline and Noncrystalline Components. Figure 3a shows $T_{1\rho\text{H}}$ decays for the ¹³C CH signals for the α sample at various temperatures. At 25 °C (well below T_g) and 67 °C, the relaxation curves show apparently single exponential behaviors with the best fit $T_{1\rho\text{H}}$ value of (86 ± 3) ms and (65 ± 5) ms, respectively. At 103 and 115 °C, double exponential curves were clearly observed. The initial decaying parts were expanded and inserted into Figure 3a. The best-fit curves to the experimental data produced $T_{1\rho\text{H}} = (3 \pm 2)$ ms (fraction, $f = 5\%$) and (157 ± 19) ms at 103 °C and $T_{1\rho\text{H}} = (0.3 \pm 0.2)$ ms ($f = 6\%$) and (110 ± 9) ms at 115 °C. The observed relaxation behaviors can be explained in terms of different contributions of the amorphous and crystalline relaxations as a function of temperatures: For example at 103 °C, the clearly observed minor and major components are attributed to the amorphous and crystalline relaxations, respectively. Also, due to the different CP efficiency which suppresses the mobile part more, the final obtained spectra contain a much less amorphous component at high temperatures ($>T_g$). The short time value of 3 ms is attributed to thermally activated segmental motions in the amorphous region at temperatures well above T_g . The large relaxation contrast between the crystalline and amorphous regions indicates that the motional frequency in the amorphous regions is much faster than that in the crystalline region. Linear combinations of two CPMAS NMR spectra with and without $T_{1\rho\text{H}}$ filters with a pulse length of 4 ms, thus, provides the possibility to extract spectra of pure amorphous and crystalline components separately, as shown in Figure 3b. On the other hand, the single exponential curve at temperatures below 67 °C means that the $T_{1\rho\text{H}}$ values for the amorphous and crystalline regions are not much different between each other, due to the decreased segmental mobility in the amorphous regions. An interesting result is the longer $T_{1\rho\text{H}}$ value at 67 °C (86 ms) as compared to that at 25 °C (65 ms). This unique behavior could be explained in terms of several reasons. First, contribution of the amorphous signals to the CPMAS spectra varies as a function of temperature: they significantly contribute to the spectra with decreasing temperature due to the increased CP efficiency. Thus, the relative amounts of the amorphous signals to the crystalline ones in the CPMAS spectra heavily contribute to the relaxation curves at 25 °C. Another effect is spin diffusion between the crystalline and amorphous regions. Spin diffusion is efficient at temperatures below T_g and leads to an averaging of the $T_{1\rho\text{H}}$ values of the different phases. These two reasons can reasonably explain the apparently shorter $T_{1\rho\text{H}}$ values at 25 °C than that at 67 °C. Later on, we will investigate the slow dynamics of PLLA crystalline chains using CODEX sequences in which a $T_{1\rho\text{H}}$ filter (62.5 kHz) with a spin-locking time of 4 ms was incorporated to suppress the amorphous signals.

3.3. CSA. Figure 4 shows the ¹³C CP NMR spectra of the α sample without MAS at 25 °C. In the case of PLLA, a simple CP spectrum shows the chemical shift anisotropy (CSA) spectrum of all three functional groups without any serious

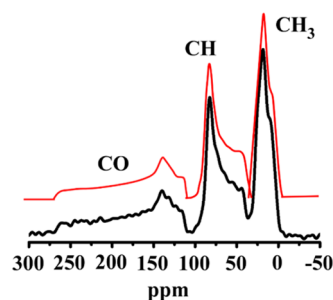


Figure 4. Experimental and calculated ¹³C CSA NMR patterns for C(=O), C(H), and C(H₃) of PLLA in the α sample at 25 °C. Lorentzian line broadening of 3 ppm was applied to the calculated the CSA line shapes.

overlapping among the peaks. Thus, simple static CP spectra provide the principal values of ¹³C CSA through powder-pattern analysis. The best-fit calculated CSA patterns of the three carbons are also depicted as red curves in Figure 5. The

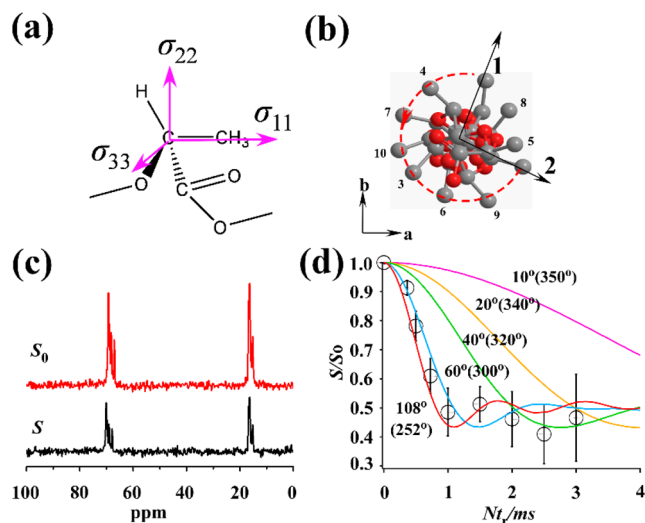


Figure 5. (a) Schematic illustration of the ¹³C CSA tensor orientations of the methine carbon based on the literature result.⁴⁵ (b) The uniform left-handed 10₇ PLLA helix projected onto the a - b plane. (c) $T_{1\rho\text{H}}$ filtered CODEX S and S_0 spectra for the α phase with $N_{\text{tr}} = 2.5$ ms and $t_{\text{mix}} = 100$ ms at 115 °C. (d) The experimental (O) and simulated CODEX N_{tr} dependence of the (S/S_0) curves of the methine carbon based on various reorientation angles $\varphi = 10^\circ$ (350°), 20° (340°), 40° (320°), 60° (300°).

obtained principal values (σ_{11} , σ_{22} , σ_{33}), together with the asymmetry parameter, η , are listed in Table 1. Later, this CSA parameter will be used for analysis of CODEX data for the PLLA α phase.

Pawlak et al. determined the orientations of the principal axes of the C(H) and C(=O) groups of PLLA using density

Table 1. Principal Values of the Shielding Tensor of ¹³C CSA

		σ_{11} (ppm)	σ_{22} (ppm)	σ_{33} (ppm)	σ_{iso} (ppm)	η^a
α	C(=O)	113	133	264	170	0.21
	C(H)	85	79	43	69	0.27
	C(H ₃)	32	19	3	18	0.87

^aThe asymmetry parameter $\eta = |\sigma_{11} - \sigma_{22}|/|\sigma_{33} - \sigma_{\text{iso}}|$.^{10,47}

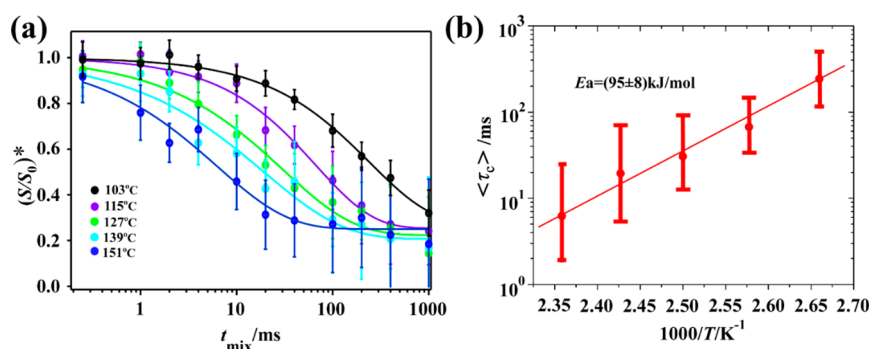


Figure 6. (a) t_{mix} dependence of $T_{1\rho\text{H}}$ filtered CODEX $(S/S_0)^*$ decay curves with the recoupling time and $Nt_r = 2$ ms for the CH groups of the PLA in the α phase. (b) Arrhenius plot of the average correlation time $\langle \tau_c \rangle$ as a function of temperature.

functional theory (DFT) calculations.⁴⁵ For the CH carbon, the σ_{11} direction aligns along the C(H)–CH₃ bond, the σ_{22} direction remains in the plane formed by H–C(H)–CH₃, and the σ_{33} direction is vertical to the plane constructed by σ_{11} and σ_{22} , respectively, as depicted in Figure 5a.

At 25 °C, the PLLA backbone does not undergo any molecular motions relevant to CSA reorientations.⁴⁵ Thus, we can reasonably assume that the obtained CSA principal values are the rigid limit values and that they can be used for analyzing PLLA backbone dynamics in the crystalline region at higher temperatures.

3.4. Dynamic Geometry of PLLA Chains in the α Phase. The geometries of the molecular motions for the PLLA backbone in the α phase were investigated on the basis of the evolution-time dependence of $T_{1\rho\text{H}}$ filtered CODEX at 115 °C. Figure 5c shows reference and exchange spectra at $t_{\text{mix}} = 100$ ms and $Nt_r = 2.5$ ms. The decrease in both the CH and CH₃ signal intensities in the exchange spectrum compared with those in the reference spectrum indicates that the chains in the 10₇ helix undergo overall motions within a dynamic window of 100 ms at 115 °C. For the CO group, however, even the reference signal S_0 at $Nt_r = 2.5$ ms is almost invisible which arises from strong signal decay due to a short T_2 value of CO group and low CP efficiency. Thereby, molecular dynamics analysis was achieved using the CH group in CODEX experiments.

Figure 5d illustrates the Nt_r dependence of the (S/S_0) intensities (black open circles) of the CH signal of the PLLA α phase with $t_{\text{mix}} = 100$ ms at 115 °C and compares it with simulation results of the 10₇ helix at various jump angles around the helical axis. The simulation of the CODEX decay curves is based on the CSA principal-axis orientation (X^{PAS} , Y^{PAS} , Z^{PAS}) (Figure 5a) and the reorientation angles because of the molecular motions, as described by Euler angles.^{8,10} The reorientation of the PAS in the molecular frame (MF) (consisting of X^{MF} , Y^{MF} , and Z^{MF} , where Z^{MF} is aligned with the chain axis) can be described by the change in the Euler angles from $(\alpha, \beta, 0)$ to (α, β, φ) , where α is the angle of the rotation of the Y^{PAS} to the node line, which is normal to Z^{PAS} and Z^{MF} , and β is the angle between Z^{PAS} and Z^{MF} .¹⁰ These two angles are determined by the helical conformations, and φ is the reorientation angle of the helical chains. Actually, the Euler angles for all 10 sites are different due to the conformationally disordered 10₇ helix of PLLA in the α phase. In our simulations, we calculated the evolution time dependence of the CODEX decaying curves at all 10 sites and plot the averaged results in Figure 5d. The simulation curves change sensitively as a function of the jump angle φ when φ values are less than 60°,

whereas larger angles than 60° do not largely change the Nt_r dependence of the (S/S_0) curves. The calculated averaged curves with $\varphi = (235^\circ\text{--}269^\circ)$, $\alpha = (54^\circ\text{--}75^\circ)$, and $\beta = (22^\circ\text{--}55^\circ)$ (red curve) are based upon the helical jump angle for a 10₇ helix. Comparison of the experimental and the simulation results indicates that the 10₇ helix performs helical jump motions, even though the different jump angles are closely consistent with the experimental results. Notably, the plateau value of ~ 0.5 was obtained at $t_{\text{mix}} = 100$ ms at 115 °C. This finding indicates that helical jump motions dominantly prefer two site jumps between next-neighboring sites within a dynamic window of 100 ms. However, as it will be shown below, this figure changes at a larger time window, revealing that sites beyond the next neighbor are reached.

3.5. Correlation Time for Molecular Motions of PLLA in the α Phase. Figure 6a shows the t_{mix} dependence of $T_{1\rho\text{H}}$ filtered CODEX $(S/S_0)^*$ curves with $Nt_r = 2$ ms for the methine carbon of PLLA in the α phase at 103–151 °C, where * means that a spin-diffusion correction was applied to the experimental CODEX decays. The recoupling time Nt_r is set beyond 1.5 ms to ensure a correct interpretable plateau value (Figure 5). The spin diffusion data were obtained at 25 °C and a S/S_0 of CH signal at a maximum $t_{\text{mix}} = 1$ s give 0.95. CODEX $(S/S_0)^*$ decaying curves decay faster with increasing temperature which means that the observed decays are dominated by thermally activated dynamic processes of the PLLA backbone in the crystalline region. The obtained t_{mix} dependence of the CODEX data was analyzed in terms of the following equation: $(S/S_0) = 1 - a(1 - \exp(-\langle \tau_c \rangle / t_{\text{mix}}))^\beta$, where a is determined by the number of available jump sites p , $a = (p - 1)/p$; β is the width distribution; and $\langle \tau_c \rangle$ is the averaged correlation time.³⁷ The best-fit parameters for the experimental data are listed in Table 2. The best-fit a values are in the range of 0.73–0.79 at various temperatures up to 151 °C. These values indicate that the number of magnetically inequivalent sites which are reached within the given time window is close to four. The obtained $\langle \tau_c \rangle$ values at temperatures of 103–151 °C were plotted as

Table 2. CODEX Best-Fit Parameters for Helical Jump Motions of the PLLA α Phase at Various Temperatures

temp/°C	a	β	$\langle \tau_c \rangle$ /ms
103	0.73 ± 0.04	0.68 ± 0.05	243 ± 46
115	0.75 ± 0.03	0.73 ± 0.08	67 ± 11
127	0.78 ± 0.04	0.59 ± 0.08	31 ± 8
139	0.79 ± 0.04	0.53 ± 0.09	19 ± 6
151	0.76 ± 0.12	0.58 ± 0.08	6 ± 1

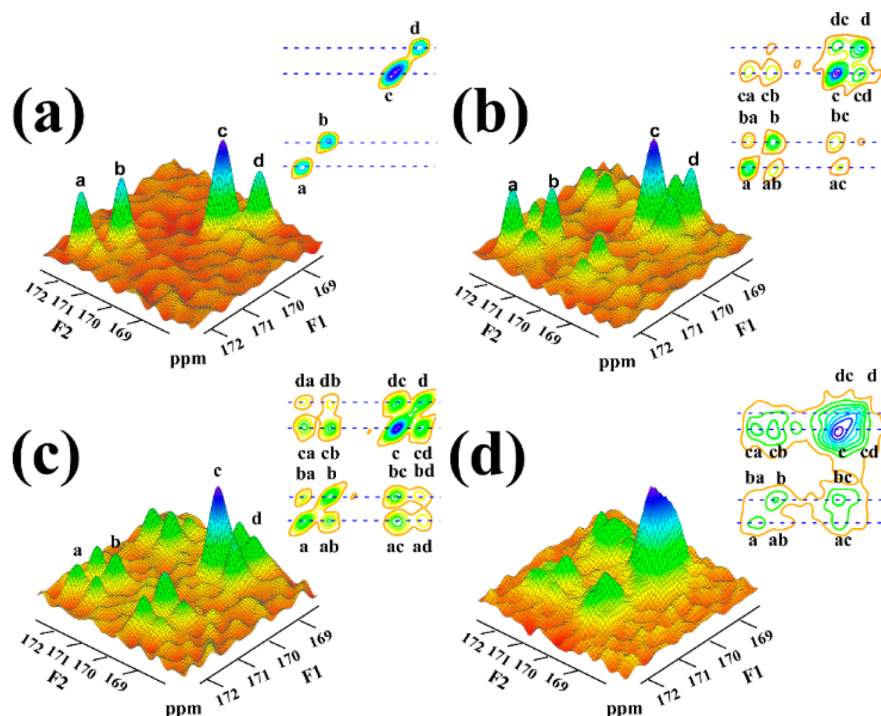


Figure 7. 2D ^{13}C exchange NMR spectra of the carbonyl region with a MAS spinning frequency of 4 kHz at 115 $^{\circ}\text{C}$ with $t_{\text{mix}} = 1$ (a), 200 (b), and 1000 ms (c). (d) Exchange NMR data taken with $t_{\text{mix}} = 200$ ms at 133 $^{\circ}\text{C}$ for comparison and discussion of spin-diffusion effect.

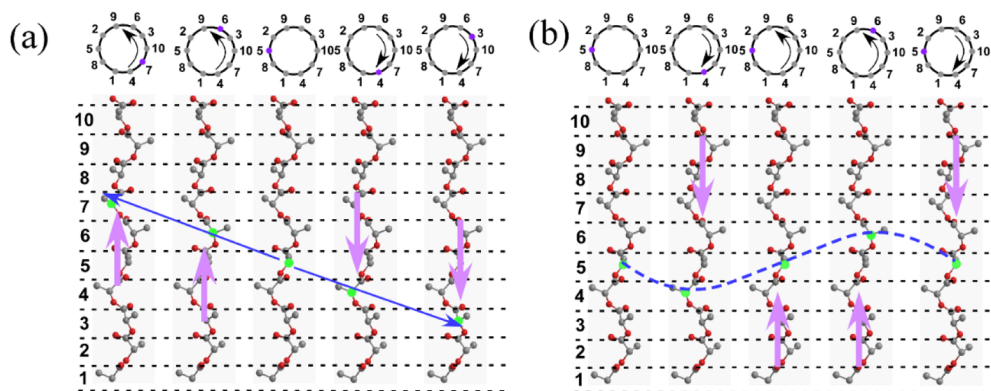


Figure 8. Two jump models of PLLA within the crystalline region: (a) one direction sliding (scenario 2) and (b) statistical back-and-forth or Markov process (scenario 3).

open circles in Figure 6b. The bars actually are not error bars but mean the distribution width of $\langle\tau_c\rangle$ as calculated from the β value.⁴⁸ The temperature dependence of $\langle\tau_c\rangle$ shows an Arrhenius behavior with an activation energy of E_a of (95 ± 8) kJ/mol. The obtained E_a value is quite similar to the reported E_a values for the crystalline chain dynamics in various semicrystalline polymers (e.g., 102 and 75 kJ/mol for the α_1 and α_2 phases of iPP,⁶ and 122 kJ/mol for PE³).

3.6. Short-Range Correlations of Helical Jump Motions. The t_{mix} and evolution-time dependence of CODEX provide kinetics and geometry information, respectively, of the molecular motions for PLLA chains in the crystalline region. Pure CODEX data clearly indicate that thermally activated helical jump motions dominate CODEX decaying curves as a function of temperature. However, it is difficult to learn about couplings of successive jumps from 1D-CODEX data alone. The only hint so far is the plateau values of the CODEX data which indicate that a given monomeric

segment can occupy sites beyond the next neighbor. However, since the chain conformations result in multiply split peaks and thus in a spectroscopic resolution of the different sites, 2D-MAS exchange experiments might help to provide more information about details of the dynamic coupling between neighboring monomeric units. The build-up and down curves of the cross and diagonal peaks, respectively, allow us to investigate the short-range coupling of the individual helical jumps of the PLLA chains in the crystalline region.

Figure 7 shows the t_{mix} dependence of the ^{13}C 2D exchange NMR spectra of the carbonyl carbon at 115 $^{\circ}\text{C}$. At $t_{\text{mix}} = 1$ ms, only the four diagonal peaks *a*, *b*, *c*, and *d* were observed. At a $t_{\text{mix}} = 200$ ms, the cross peaks originating from spin exchange due to the helical jump motions between the neighboring sites are clearly observed. The appearance of these 4 major cross peaks confirms former signal assignments by Pawlak et al.⁴⁵ With increase of the t_{mix} up to 1000 ms, in addition to the further increase of the *ab*, *ac*, *bc*, and *cd* peaks, new cross peaks

of *ad* and *bd* corresponding to spin exchange to the second and third closest neighbors, respectively, are also observed. The t_{mix} dependence of the cross peak intensities between the original and the first, the second, and the third neighbors include information about how helical jump motions are correlated with each other. One may argue another spin exchange process due to spin diffusion. In the case of CODEX, we calibrated spin-exchange effects using CODEX data at a quite low temperature below T_g , where molecular dynamics is frozen. Here, we measured the 2D exchange spectrum with $t_{\text{mix}} = 200$ ms at 133 °C (Figure 7d). It is clearly seen that the cross peak intensities at 133 °C is much stronger than that with the same t_{mix} at 115 °C. The enhanced cross peak intensity supports that the dynamic process dominates the cross peak intensities.

We will express the degree of coupling by the deviation of the dynamic process from Markov behavior,⁴⁹ which states that a given jump event is independent from the previous one. With this, one could imagine three scenarios:

1. After a helical jump of a given monomeric to its neighboring site, it will only jump back to the site it started from. Such a process will actually lead only to cross peaks of the type *ab*, *ac*, *bc*, and *cd* but never to *ad* and *bd* cross peaks. Thus, this model is already ruled out by the 2D data.
2. After a helical jump of a given monomeric to its neighboring site, it will always jump forward or backward to occupy the next site, i.e. the next position in the helix as illustrated in Figure 8a. Basically, this would be in agreement with the appearance of *ad* and *bd* cross peaks but cannot be proven from that fact alone.
3. After a helical jump of a given monomeric to its neighboring site, the next jump is completely uncorrelated to the previous one (random jump) and is thus well described by Markov statistics as illustrated in Figure 8b. This process will also lead to *ad* and *bd* cross peaks, but the time evolution of them will be different as in case 2: the population of these sites will take a longer time as compared to scenario 2.

Thus, the time evolution of the appearance of the different 2D cross peaks will reveal the details of the dynamic process. To calculate the t_{mix} dependence of the diagonal and off-diagonal intensities, the t_{mix} dependence of the magnetization at individual sites must be known. The deviation of the magnetization under *N*-site exchange can be expressed as:⁵⁰

$$\begin{aligned} \frac{dm_i}{dt} = & k_{1i}m_1 + k_{2i}m_2 + \dots - (T_{1,i}^{-1} + \sum_l^n k_{il})m_i \\ & + \dots + k_{ni}m_n \end{aligned} \quad (1)$$

where $k_{ij}m_i$ indicates the magnetization transfer from site *i* to *j*, and $T_{1,i}$ is the spin–lattice relaxation time of site *i*. The $T_{1,i}$ values are 39, 43, 39, and 40 s at 115 °C in the order *a* to *d*, respectively. For simplification, eq 1 can be written in matrix form as $\dot{\mathbf{m}} = -\mathbf{Rm}$, which means:

$$\frac{d\mathbf{m}}{dt} = -\mathbf{Rm} \quad (2)$$

The component of R_{ij} in matrix **R** is given by:

$$R_{ij} = \begin{cases} -k_{ji} (i \neq j) \\ T_{1,i}^{-1} + \sum_l^n k_{il} (i = j) \end{cases} \quad (3)$$

The analytical solution of function (2) is difficult for *N*-site exchange ($N > 3$), but the numerical one can be achieved through:

$$-\delta\mathbf{m}(t) = \mathbf{Rm}(t) \delta t$$

Then

$$\mathbf{m}(t + \delta t) = (1 - \mathbf{R} \delta t) \mathbf{m}(t) \quad (\delta t \cdot \max(k, T) < 1) \quad (4)$$

Once the initial values of $\mathbf{m}(t_{\text{mix}} = 0)$ and the kinetic matrix **R** are known, the magnetization $\mathbf{m}(t_{\text{mix}})$ as a function of the mixing time t_{mix} can be calculated. For the carbonyl carbon, the initial $\mathbf{m}(t_{\text{mix}} = 0)$ for peak *a* can be represented in terms of $\mathbf{m}(t_{\text{mix}} = 0) = [1 \ 0 \ 0 \ 0]$. The kinetic matrix **R** for two different models is rather different. For the statistical back–forth model (scenario 3), **R** can be represented as:

$$\mathbf{R}_1 = k_0 \begin{bmatrix} 2 & -1 & 0 & -1 & 0 \\ -1 & 2 & -1 & 0 & 0 \\ 0 & -1 & 2 & 0 & -1 \\ -1 & 0 & 0 & 2 & -1 \\ 0 & 0 & -1 & -1 & 2 \end{bmatrix} \quad (5)$$

and

$$k_0 \langle \tau_c \rangle = 1/n \quad (6)$$

where *n* is the available site number of helical jump motions. For the one direction sliding model (scenario 3), **R** can be separately expressed for the back-and-forth jump:

$$\mathbf{R}_2(\text{Forth}) = k_0 \begin{bmatrix} 1 & 0 & 0 & -1 & 0 \\ -1 & 1 & 0 & 0 & 0 \\ 0 & -1 & 1 & 0 & 0 \\ 0 & 0 & 0 & 1 & -1 \\ 0 & 0 & -1 & 0 & 1 \end{bmatrix} \quad (7a)$$

$$\mathbf{R}_2(\text{back}) = k_0 \begin{bmatrix} 1 & -1 & 0 & 0 & 0 \\ 0 & 1 & -1 & 0 & 0 \\ 0 & 0 & 1 & 0 & -1 \\ -1 & 0 & 0 & 1 & 0 \\ 0 & 0 & 0 & -1 & 1 \end{bmatrix} \quad (7b)$$

These two kinetic matrixes are asymmetric due to different moving directions. The build-up curves based on eqs 7a and 7b are independently calculated. Then, an averaged curve for the two build-up curves are used as the preference in the case of one-direction sliding.

A least-squares fitting is used here to match the simulated curves to the experimental data and extract kinetic parameters. The error *R* between the simulation and the experimental results is defined as follows:

$$R = \sqrt{\sum_i \sum_j (E_{ij} - S_{ij})^2} \quad (1 \leq i, j \leq 4) \quad (8)$$

where E_{ij} and S_{ij} represent the experimental and simulated exchange intensities, respectively, from site *i* to *j*. Here, the

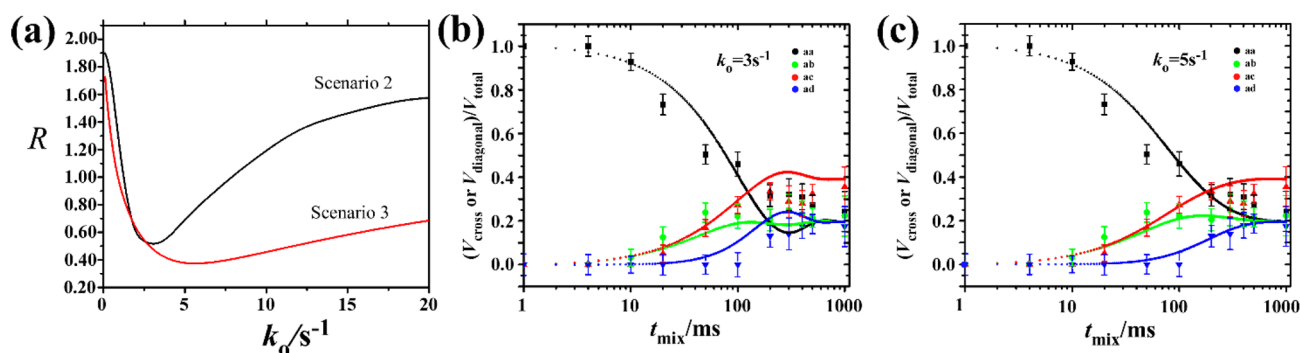


Figure 9. (a) k_0 dependence of the R values calculated based on eq 8 in both scenario 2 (black curve) and 3 (red). t_{mix} dependence of the normalized cross and diagonal peaks at a site and simulated buildup and down curves for (b) scenario 2 “one-direction model” ($k_0 = 3$ s⁻¹) and (c) scenario 3 “statistical back-and-forth model” ($k_0 = 5$ s⁻¹).

NMR exchanges between site c_1/c_2 and other sites are converted into one intensity buildup curve, since the four well resolved peaks are observed. The normalized volumes for the cross and off diagonal peaks are plotted in Figure 9b and c, where the normalization was obtained by dividing the diagonal (V_{diag}) or cross peak volumes (V_{cross}) by those of the total peaks (V_{total}). The error R values were calculated for the a site as a function of k in both scenarios of 2 and 3, and shown in Figure 9a. In the latter, the best-fit results to the experimental data were obtained at $k_0 = 5.0 \pm 0.5$ s⁻¹ with $R = 0.39$ (see Figure 9a). The decay of the normalized aa diagonal peak and the increase of the normalized individual cross peaks give good consistencies with the experimental decaying and increasing peak volumes in the whole t_{mix} range as shown in Figure 9c. For scenario 2, the best-fit curves were obtained at $k_0 = 3$ s⁻¹ with $R = 0.52$ as shown in Figure 9b. The calculated and experimental data show good consistencies at t_{mix} up to 100 ms. However, the calculated curves for the normalized aa , ac , and ad peaks show deviations from their experimental results at a longer t_{mix} than 100 ms. Among the 4 curves, the buildup curve of the ad peak corresponding to jumps to the second neighbors shows the largest deviations. The calculated curve for the ad peak shows similar buildup behavior for the ac peak, whereas the experimental ad peak shows slower behaviour than that for the ac peak. In addition, the calculated curves show small bumps for both the cross and diagonal peaks at around 300 ms. These bumps arise from 5 successive helical jumps which return the occupied sites to the original ones. Such bumps were not observed in experimental results. Comparisons of the experimental results and the calculated results on the basis of two models clearly indicate that local helical jumps prefer random back-and-forth jumps and individual jumps are not effectively coupled with each other.

The determined k_0 value of 5 s⁻¹ is the single-jump exchange rate for helical jumps. Taking $n = 5$, $k_0 = 5$ s⁻¹ corresponds to $\langle \tau_c \rangle = 40$ ms using eq 6. This is very consistent with $\langle \tau_c \rangle = 67 \pm 11$ ms determined by CODEX at the same temperature. Besides, 2D exchange buildup curves also reach equilibrium states at approximately $t_{\text{mix}} = 1$ s. This means that helical jump motions occupy five available sites within 1 s. The number of the available sites is very consistent with the number 4 as obtained by CODEX. 2D exchange and CODEX decaying curves give similar results about available dynamic sites and $\langle \tau_c \rangle$. Considering the nature of random back-and-forth motions of PLLA chains, it is easily understood that long-range traveling

within 10 sites would take a longer time than the current dynamic window.

4. DISCUSSION

4.1. Structural Factor Effects on Molecular Dynamics in the Crystalline Region. So far, SS-NMR works demonstrated that several polyesters including poly(ethylene terephthalate) (PET)⁵¹ and poly(caprolactone) (PCL)⁵² are fixed crystals. A series of CODEX and 2D exchange experiments in this study clearly indicated that PLLA α -crystals are α_c mobile. In the review by Hu and Schmidt-Rohr,¹¹ it was pointed out that several structural factors, including conformation, repeating monomer length, packing, chemical interactions, lamellae thickness, etc., determine in a complex manner whether the crystals are either α_c mobile or fixed. Here we consider the structural similarity and difference among PLLA, other mobile, and fixed polyester crystals and try to understand structural origins governing the mobility of the crystalline chains. PLLA α crystals have similar conformations with reported mobile crystals including *i*PP (3₁ helix),^{6,7} *i*P4M1P (7₂ helix),^{8,39} POM (9₅ helix),² etc. They commonly adopt helical conformations, where *gauche* or nearly *gauche* conformations effectively shorten the monomeric lengths along the c axis. For example, PLLA and *i*PP show 2.88 and 2.16 Å, respectively. On the other hand, PCL and PET have larger backbone atomic numbers than that for PLLA and adopt extended chain conformations and show monomeric lengths of 8.58 and 10.76 Å, respectively. The longer monomeric lengths along the chain axis lead to large energy barriers for translations and rotations of the chains within the crystalline regions. The conformational and monomeric length difference would significantly influence the stem mobility in the crystalline regions.

The second factor is the packing structure. The PLLA α form is a chiral crystal where PLLA chains possess chiral centers and configurationally adopt only left handed chains. Simple polyolefins such as *isotactic*-poly(1-butene) (*i*PB1) do not have a chiral center and can adopt either right or left handed chains. As a result, *i*PB1 can crystallize as either chiral or racemic crystals depending on the crystallization conditions. Very recently, Miyoshi et al. systematically investigated the molecular dynamics of *i*PB1 in a different polymorph.^{9,38} The most stable form, I (3₁ helix in racemic trigonal packing with $\rho = 0.920$ g/cm³), does not show helical jump motions up to its T_m while form III (4₁ helix in chiral orthorhombic crystals ($\rho = 0.897$ g/cm³)) shows helical jump motions in an intermediate

range (\sim kHz range) even at room temperature. This is one example of how a chain packing difference influences the molecular dynamics of the crystalline chains in chiral and racemic crystals. Thermodynamically stable racemic crystals give tighter packing with a higher T_m than those of chiral crystals. From views of packing structures, it is reasonably explained why PLLA α crystals are mobile. As explained in the Introduction, PLLA also shows polymorphs and forms stereo complexes (SC) with PDLA (right handed helices) with a higher T_m of 220 $^{\circ}\text{C}$.⁵³ It would be definitively interesting to investigate the molecular dynamics of PLLA in thermodynamically stable racemic SC crystals. Research related to such a topic is under investigation and will be published elsewhere.

Third, an intermolecular interaction is also a very important factor. PET, PCL, and PLLA include an ester group which is a hydrogen acceptor. However, all three do not include hydrogen donor function. Thereby, CO groups do not strongly interact with other functional groups. Among the three polyesters, only the PET includes aromatic rings in the backbone, which can cooperatively form π - π stacking in the crystalline region,⁵⁴ which would significantly restrict the molecular dynamics of PET in the crystalline region.

At last, the lamellar thickness effect is considered. According to literature, fixed crystals of PET (8–12 nm)⁵⁵ and PCL (10 nm)⁵⁶ show similar lamellar thicknesses as compared with that for the α phase of PLLA (\sim 12 nm at $T_c = 140$ $^{\circ}\text{C}$).⁵⁷ Considering these facts, the thickness does not play an important role in the determination of either fixed or mobile crystals in the crystalline regions among the three polyesters.

Through these discussions, it is reasonably concluded that the conformation, monomer unit length, and lateral packing are the most important structural factors which can lead to largely different backbone mobility among the three polyesters.

4.2. DRS vs SS-NMR. Another discussion point on PLLA dynamics is the different conclusion drawn by former dielectric relaxation spectroscopy (DRS)³¹ and current SS-NMR. The reported DRS studies have mainly focused on the molecular dynamics of the amorphous components for the semicrystalline PLLA samples at temperatures above the T_g . Brás et al. noted that no crystalline relaxation of PLLA occurs within a wide frequency range of 0.1 Hz to 10 MHz, in the temperature range of 100 to 170 $^{\circ}\text{C}$.³¹ Therefore, no mismatch of the frequencies and temperatures occurs between DRS and SS-NMR; rather, mechanisms of the relaxation process in the crystalline regions might greatly influence different views on the molecular dynamics between the two techniques. The DRS method can detect relaxations and orientations of dipole moments under changing electric field directions and has been successfully used to investigate the local, segmental, and overall dynamics of amorphous polymers. In the crystalline phases, conformations of polymer chains are well-defined because of their regular and tight packing with neighboring chains. The detected slow dynamics of PLLA in the crystalline form and other semicrystalline polymers by SS-NMR commonly are helical jump motions including jump rotations and translations, which do not change the net dipole moments per stem before and after the jumps. Therefore, DRS cannot detect such molecular dynamics. This inability to be detected by DRS may be the reason why previous DRS studies could not detect helical jump motions of PLLA in the crystalline region. To our best knowledge, only one exceptional case for the detection of PE crystalline dynamics by DRS has been reported.⁵⁸ In that work, the molecular dynamics of the C=O group of the oxidized PE

was investigated. The relaxation map obtained by DRS is consistent with that obtained by recent 2D exchange NMR data.¹² Most likely, the C=O groups of oxidized PE would locate at nonsymmetric crystallographic sites in the crystalline region and/or at the interfacial regions near the crystalline region.

4.3. Short-Range Correlations of Local Jump Motions in Semicrystalline Polymers. Here, we would like to comment on the local and long-range dynamics of semicrystalline polymers. According to literature,^{3,12–18} PE chains perform both local flips and long-range chain diffusions. However, the relationship between local flips and chain diffusions is still unclear. Yao et al.¹⁷ reported that chain diffusions in the melt-grown of PE shows the same E_a value of 50 kJ/mol as that in the solution-grown crystals under the assumption of the free chain diffusion model, and the E_a value for chain diffusions is much smaller than that for the local flips (122 kJ/mol) determined by Hu et al.³ On the basis of the different E_a values between the local chain flips and chain diffusions, Spiess related the former to defect traveling and the latter to twist modes of entire stems.⁵⁹ Very recently, Bärenwald et al. also succeeded in measuring the local flip rates of PE in different morphologies including nanodisks, reactive powders, and melt-grown crystals by using ^1H magic sandwich echo without isotopic labeling.¹³ After correction of the correlation time,¹⁸ they reported E_a values of 61–114 kJ/mol for the local flips of PE in different morphologies. The E_a value for the local flips in the melt-grown crystals was very consistent with the former result by Hu et al.³ They also reported that effective diffusion coefficients (D) estimated by local flip rates are much faster than the D values determined by ^{13}C polarization transfer. This trend is very consistent with the results by Yao et al.¹⁷ However, Bärenwald et al. pointed out that the free diffusion models used by Yao et al.¹⁷ and themselves^{13,18} might underestimate the D values at high temperatures and lead to smaller E_a values. In fact, Schmidt-Rohr and Spiess reported the E_a value of 105 kJ/mol for the chain diffusion of PE under the assumptions of the constrained chain diffusion due to entanglements.¹² This realistic model provided a very similar E_a value with those for the local flip motions.^{3,18} This fact simply implies that one dynamic process governs both short- and long-range dynamics of PE chains in the crystalline regions.

As demonstrated in this work, local helical jump motions of PLLA chains are dominated by statistical back-forth jump motions (scenario 3) as similarly observed in POM drawn samples by Schmidt-Rohr and Spiess.^{10,19} The fact that two different α_c mobile polymers show back-and-forth motions implies that local back-and-forth jump motion is common dynamics in α_c mobile crystals. Back-and-forth motions can reasonably explain differences between the local flip rates and effective flip rates estimated from chain diffusions by Yao et al. and Bärenwald et al. Very similar E_a values for the local flips determined by Hu et al.³ and chain diffusions by Schmidt-Rohr and Spiess¹² would also support our opinion.

In this study, we analyzed 2D exchange data in terms of a Markov process which can generally describe molecular diffusions. However, it is questionable whether the Markov process simply holds for describing unique chain diffusions of long polymer chains across both the crystalline and amorphous regions, because the amorphous structures including chain folding (tight vs loose loop), tie molecules, cilia, and entanglements are likely to influence the chain diffusions as pointed out by Schmidt-Rohr and Spiess.¹² Besides, Yao et al.

pointed out the importance of the local order of the segments at the interface in the melt- and solution-grown crystals.¹⁵ This interfacial order is generated by constraints of the chain-folding structures. However, detailed chain-folding structures of semicrystalline polymers are still controversial in literature.⁶⁰ Very recently, our group developed a ¹³C–¹³C double quantum (DQ) NMR strategy to access the chain-folding structures of a semicrystalline polymer and revealed that iPB1 possesses adjacent re-entry rich structures in both single- and melt-grown crystals, although the former has an increased long-range order than that of the latter.^{61,62} As shown in this study, PLLA is one of the best samples to study the morphological effects on local jumps and their correlations. Currently, further work on the molecular dynamics as well as chain-folding analysis of PLLA in different morphologies are under progress. Comparisons of molecular dynamics and molecular level structures in the melt-grown crystals with the solution-grown crystals will help in understanding the morphological effects on the local dynamics of helical jump motions in semicrystalline polymers.

5. CONCLUSION

We have successfully investigated the molecular dynamics of the crystalline chains of PLLA in the α phase by CODEX and 2D-exchange NMR. The evolution-time dependence of the CODEX data revealed that PLLA helices perform helical jump motions as similarly observed in α_c mobile crystals such as PE, iPP, PEO, etc. Such dynamic character significantly influences the mechanical property of PLLA at high temperature.²⁷ The CODEX mixing-time dependence provides correlation times of helical jump motions at various temperatures, and the Arrhenius plot of $\langle\tau_c\rangle$ yields an activation energy of (95 ± 8) kJ/mol. These experimental results reject the former DRS conclusion suggesting there is no crystalline relaxation in the α phase of PLLA. 2D exchange NMR based on exchange between isotropic chemical shifts detected spin exchange between multiple sites due to helical jump motions. Experimental build-up curves and numerical simulations demonstrated that helical jump motions of PLLA are dominated by statistical back-and-forth jump motions. There are several reports on morphological effects on the molecular dynamics of PE; however, consistent conclusions are still not drawn. To draw clear conclusions of the morphological effects on molecular dynamics at different length scales, short-range correlations of the individual local jumps are necessary in different morphologies with well controlled structures (e.g., lamellae thickness, chain-folding structures, and entanglements). To fully understand the relationship between structure and dynamics, more elaborate efforts on not only dynamics but also structural parts at the molecular level are necessary.

AUTHOR INFORMATION

Corresponding Author

*E-mail: miyoshi@uakron.edu.

Notes

The authors declare no competing financial interest.

ACKNOWLEDGMENTS

This work was financially supported by the National Science Foundation (Grant Nos. DMR-1105829 and 1408855) and by UA startup funds. We are thankful to Dr. Kay Saalwächter for providing helpful comments.

REFERENCES

- (1) Hoffman, J. D.; Williams, G.; Passaglia, E. Analysis of the α , β , and γ Relaxations in Polychlorotrifluoroethylene and Polyethylene: Dielectric and Mechanical Properties. *J. Polym. Sci. Part C* **1966**, 235, 173–235.
- (2) Kentgens, A. P. M.; de Boer, E.; Veeman, W. S. Ultraslow molecular motions in crystalline polyoxymethylene. A complete elucidation using two-dimensional solid state NMR. *J. Chem. Phys.* **1987**, 87, 6859–6866.
- (3) Hu, W.-G.; Boeffel, C.; Schmidt-Rohr, K. Chain Flips in Polyethylene Crystallites and Fibers Characterized by Dipolar ¹³C NMR. *Macromolecules* **1999**, 32, 1611–1619.
- (4) Schaefer, D.; Spiess, H. W.; Suter, U. W.; F, W. W. Two-Dimensional Solid-state NMR Studies of Ultraslow Chain Motion: Glass Transition in Atactic Poly(propylene) versus Helical Jumps in Isotactic Poly(propylene). *Macromolecules* **1990**, 23, 3431–3439.
- (5) Kang, J.; Miyoshi, T. Two Chain-Packing Transformations and Their Effects on the Molecular Dynamics and Thermal Properties of α -Form Isotactic Poly(propylene) under Hot Drawing: A Solid-State NMR Study. *Macromolecules* **2014**, 47, 2993–3004.
- (6) Li, Z.; Miyoshi, T.; Sen, M. K.; Koga, T.; Otsubo, A.; Kamimura, A. Solid-State NMR Characterization of the Chemical Defects and Physical Disorders in α Form of Isotactic Poly(propylene) Synthesized by Ziegler–Natta Catalysts. *Macromolecules* **2013**, 46, 6507–6519.
- (7) Miyoshi, T.; Mamun, A.; Hu, W. Molecular Ordering and Molecular Dynamics in Isotactic-Polypropylene Characterized by Solid State NMR. *J. Phys. Chem. B* **2010**, 114, 92–100.
- (8) Miyoshi, T.; Pascui, O.; Reichert, D. Slow Chain Dynamics in Isotactic-poly(4-methyl-1-pentene) Crystallites near the Glass Transition Temperature Characterized by Solid-State ¹³C MAS Exchange NMR. *Macromolecules* **2004**, 37, 6460–6471.
- (9) Miyoshi, T.; Hayashi, S.; Imashiro, F.; Kaito, A. Side-Chain Conformation and Dynamics for the Form II Polymorph of Isotactic Poly(1-butene) Investigated by High-Resolution Solid-State ¹³C NMR Spectroscopy. *Macromolecules* **2002**, 35, 2624–2632.
- (10) Schmidt-Rohr, K.; Spiess, H. *Multidimensional solid-state NMR and polymers*; Academic Press: London, 1994.
- (11) Hu, W.-G.; Schmidt-Rohr, K. Polymer ultradrawability: the crucial role of α -relaxation chain mobility in the crystallites. *Acta Polym.* **1999**, 50, 271–285.
- (12) Schmidt-Rohr, K.; Spiess, H. W. Chain Diffusion between Crystalline and Amorphous Regions in Polyethylene Detected by 2D Exchange ¹³C NMR. *Macromolecules* **1991**, 24, 5288–5293.
- (13) Bärenwald, R.; Goerlitz, S.; Godehardt, R.; Osichow, A.; Tong, Q.; Krumova, M.; Mecking, S.; Saalwächter, K. Local Flips and Chain Motion in Polyethylene Crystallites: A Comparison of Melt-Crystallized Samples, Reactor Powders, and Nanocrystals. *Macromolecules* **2014**, 47, 5163–5173.
- (14) Bärenwald, R.; Champouret, Y.; Saalwächter, K.; Schäler, K. Determination of Chain Flip Rates in Poly(ethylene) Crystallites by Solid-State Low-Field ¹H NMR for Two Different Sample Morphologies. *J. Phys. Chem. B* **2012**, 116, 13089–13097.
- (15) Yao, Y.-F.; Graf, R.; Spiess, H. W.; Rastogi, S. Restricted Segmental Mobility Can Facilitate Medium-Range Chain Diffusion: A NMR Study of Morphological Influence on Chain Dynamics of Polyethylene. *Macromolecules* **2008**, 41, 2514–2519.
- (16) Yao, Y.; Graf, R.; Spiess, H.; Rastogi, S. Influence of Crystal Thickness and Topological Constraints on Chain Diffusion in Linear Polyethylene. *Macromol. Rapid Commun.* **2009**, 30, 1123–1127.
- (17) Yao, Y.-F.; Graf, R.; Spiess, H.; Lippits, D.; Rastogi, S. Morphological differences in semicrystalline polymers: Implications for local dynamics and chain diffusion. *Phys. Rev. E* **2007**, 76, 060801.
- (18) Bärenwald, R.; Goerlitz, S.; Godehardt, R.; Osichow, A.; Tong, Q.; Krumova, M.; Mecking, S.; Saalwächter, K. Correction to Local Flips and Chain Motion in Polyethylene Crystallites: A Comparison of Melt-Crystallized Samples, Reactor Powders, and Nanocrystals. *Macromolecules* **2014**, 47, 7677–7678.
- (19) Spiess, H. W. Structure and Dynamics of Solid Polymers from 2D and 3D NMR. *Chem. Rev.* **1991**, 91, 1321–1338.

- (20) Sin, L. T.; Rahmat, A. R.; Rahman, W. A. W. A. *Poly(lactic Acid: PLA Biopolymer Technology and Applications*; Elsevier: Oxford, U.K., 2012.
- (21) Nyambo, C.; Mohanty, A. K.; Misra, M. Poly(lactide)-Based Renewable Green Composites from Agricultural Residues and Their Hybrids. *Biomacromolecules* **2010**, *11*, 1654–1660.
- (22) Yang, Q.; Hirata, M.; Lu, D.; Nakajima, H.; Kimura, Y. Highly Efficient Reinforcement of Poly(L-lactide) Materials by Polymer Blending of a Thermotropic Liquid Crystalline Polymer. *Biomacromolecules* **2010**, *12*, 354–358.
- (23) Bai, H.; Huang, C.; Xiu, H.; Zhang, Q.; Deng, H.; Wang, K.; Chen, F.; Fu, Q. Significantly Improving Oxygen Barrier Properties of Poly(lactide) via Constructing Parallel-Aligned Shish-Kebab-Like Crystals with Well-Interlocked Boundaries. *Biomacromolecules* **2014**, *15*, 1507–1514.
- (24) Tang, H.; Chen, J. B.; Wang, Y.; Xu, J. Z.; Hsiao, B. S.; Zhong, G. J.; Li, Z. M. Shear Flow and Carbon Nanotubes Synergistically Induced Nonisothermal Crystallization of Poly(lactic acid) and Its Application in Injection Molding. *Biomacromolecules* **2012**, *13*, 3858–3867.
- (25) De Santis, P.; Kovacs, J. Molecular conformation of poly(S-lactic acid). *Biopolymers* **1968**, *6*, 299–306.
- (26) Zhang, J.; Duan, Y.; Sato, H.; Tsuji, H.; Noda, I.; Yan, S.; Ozaki, Y. Crystal Modifications and Thermal Behavior of Poly(L-lactic acid) Revealed by Infrared Spectroscopy. *Macromolecules* **2005**, *38*, 8012–8021.
- (27) Eling, B.; Gogolewski, S.; Pennings, A. J. Biodegradable materials of poly(L-lactic acid): 1. Melt-spun and solution-spun fibres. *Polymer* **1982**, *23*, 1587–1593.
- (28) Cartier, L.; Okihara, T.; Ikada, Y.; Tsuji, H.; Puiggali, J.; Lotz, B. The frustrated structure of poly(L-lactide). *Polymer* **2000**, *41*, 8909–8919.
- (29) Ikada, Y.; Jamshidi, K.; Tsuji, H.; Hyon, S.-H. Stereocomplex Formation between Enantiomeric Poly(lactides). *Macromolecules* **1987**, *904*–906.
- (30) Wasanasuk, K.; Tashiro, K.; Hanesaka, M.; Ohhara, T.; Kurihara, K.; Kuroki, R.; Tamada, T.; Ozeki, T.; Kanamoto, T. Crystal Structure Analysis of Poly(L-lactic Acid) α Form on the Basis of the 2-Dimensional Wide-Angle Synchrotron X-ray and Neutron Diffraction Measurements. *Macromolecules* **2011**, *44*, 6441–6452.
- (31) Bras, A. R.; Malik, P.; Dionisio, M.; Mano, J. Influence of Crystallinity in Molecular Motions of Poly(L-lactic acid) Investigated by Dielectric Relaxation Spectroscopy. *Macromolecules* **2008**, *41*, 6419–6430.
- (32) Kanchanasopa, M.; Runt, J. Broadband Dielectric Investigation of Amorphous and Semicrystalline L-Lactide/meso-Lactide Copolymers. *Macromolecules* **2004**, *37*, 863–871.
- (33) Pan, P.; Yang, J.; Shan, G.; Bao, Y.; Weng, Z.; Cao, A.; Yazawa, K.; Inoue, Y. Temperature-Variable FTIR and Solid-State ^{13}C NMR Investigations on Crystalline Structure and Molecular Dynamics of Polymorphic Poly(L-lactide) and Poly(L-lactide)/Poly(D-lactide) Stereocomplex. *Macromolecules* **2011**, *45*, 189–197.
- (34) Tsuji, H.; Kamo, S.; Horii, F. Solid-state ^{13}C NMR analyses of the structures of crystallized and quenched poly(lactide)s: Effects of crystallinity, water absorption, hydrolytic degradation, and tacticity. *Polymer* **2010**, *51*, 2215–2220.
- (35) Thakur, K. A. M.; Kean, R. T.; Zupfer, J. M.; Buehler, N. U.; Doscotch, M. A.; Munson, E. J. Solid State ^{13}C CP-MAS NMR Studies of the Crystallinity and Morphology of Poly(L-lactide). *Macromolecules* **1996**, *29*, 8844–8851.
- (36) Tsuji, H.; Horii, F.; Nakagawa, M.; Ikada, Y.; Odani, H.; Kitamard, R. Stereocomplex Formation between Enantiomeric Poly(lactic acid)s. 7. Phase Structure of the Stereocomplex Crystallized from a Dilute Acetonitrile Solution As Studied by High-Resolution Solid-state ^{13}C NMR Spectroscopy. *Macromolecules* **1992**, *25*, 4114–4118.
- (37) DeAzevedo, E. R.; Hu, W.-G.; Bonagamba, T. J.; Schmidt-Rohr, K. Centerband-Only Detection of Exchange: Efficient Analysis of Dynamics in Solids by NMR. *J. Am. Chem. Soc.* **1999**, *121*, 8411–8412.
- (38) Miyoshi, T.; Mamun, A. Critical roles of molecular dynamics in the superior mechanical properties of isotactic-poly(1-butene) elucidated by solid-state NMR. *Polym. J.* **2011**, *44*, 65–71.
- (39) Miyoshi, T.; Pascui, O.; Reichert, D. Large-Amplitude Motions of Form III of Isotactic Poly(4-methyl-1-pentene) Crystallites Prior to Crystal-Crystal Transformation. *Macromolecules* **2004**, *37*, 6653–6656.
- (40) Tang, C.; Inomata, A.; Sakai, Y.; Yokoyama, H.; Miyoshi, T.; Ito, K. Effects of Chemical Modification on the Molecular Dynamics of Complex Polyrotaxanes Investigated by Solid-State NMR. *Macromolecules* **2013**, *46*, 6898–6907.
- (41) Miyoshi, T.; Hu, W.; Li, Y. Dynamic Geometry and Kinetics of Polymer Confined in Self-Assembly via Cooperative Hydrogen Bonding: A Solid-State NMR Study under Paramagnetic Doping. *Macromolecules* **2010**, *43*, 4435–4437.
- (42) Fischer, E. W.; Sterzel, H. J.; Wegner, G. Investigation of the structure of solution grown crystals of lactide copolymers by means of chemical reactions. *Kolloid-Zeitschrift und Zeitschrift für Polym.* **1973**, *251*, 980–990.
- (43) Loomis, G. L.; Murdoch, J. R.; Gardner, K. H. Poly(lactide) stereocomplexes. *Polym. Prepr.* **1990**, *31*, 55.
- (44) Bielecki, A.; Burum, D. P. Temperature Dependence of ^{207}Pb MAS Spectra of Solid Lead Nitrate. An Accurate, Sensitive Thermometer for Variable-Temperature MAS. *J. Magn. Reson. Ser. A* **1995**, *116*, 215–220.
- (45) Pawlak, T.; Jaworska, M.; Potrzebowski, M. J. NMR crystallography of α -poly(L-lactide). *Phys. Chem. Chem. Phys.* **2013**, *15*, 3137–3145.
- (46) Kittel, C.; McEuen, P. *Introduction to Solid State Physics*; Wiley: New York, 1976.
- (47) Chen, W.; Sun, H.-J.; Miyoshi, T. Unique Molecular Dynamics of Structural Elements in an Asymmetric Janus Bisamide Supramolecule Characterized by Solid-State NMR. *J. Phys. Chem. B* **2013**, *117*, 13698–13709.
- (48) Pascui, O.; Beiner, M.; Reichert, D. Identification of Slow Dynamic Processes in Poly(n-hexyl Methacrylate) by Solid-State 1D-MAS Exchange NMR. *Macromolecules* **2003**, 3992–4003.
- (49) Durrett, R. *Probability: theory and examples*, 4th ed.; Cambridge University Press, 2010.
- (50) Perrin, C. L.; Dwyer, T. J. Application of Two-Dimensional NMR to Kinetics of Chemical Exchange. *Chem. Rev.* **1990**, *2*, 935–967.
- (51) English, A. D. Macromolecular Dynamics in Solid Poly(ethylene terephthalate): ^1H and ^{13}C Solid-state NMR. *Macromolecules* **1984**, *17*, 2182–2192.
- (52) Schäler, K.; Achilles, A.; Bärenwald, R.; Hackel, C.; Saalwächter, K. Dynamics in Crystallites of Poly(ϵ -caprolactone) As Investigated by Solid-State NMR. *Macromolecules* **2013**, *46*, 7818–7825.
- (53) Tsuji, H.; Ikada, Y. Stereocomplex formation between enantiomeric poly(lactic acid)s. XI. Mechanical properties and morphology of solution-cast film. *Polymer* **1999**, *40*, 6699–6708.
- (54) Fu, Y.; Yimin, R. B.; Affholter, K. A.; Wunderlich, B. Poly(ethylene terephthalate) Fibers. 1. Crystal Structure and Morphology Studies with Full-Pattern X-ray Diffraction Refinement. *Macromolecules* **1993**, *26*, 2187–2193.
- (55) Wang, Z.-G.; Hsiao, B. S.; Sauer, B. B.; Kampert, W. G. The nature of secondary crystallization in poly(ethylene terephthalate). *Polymer* **1999**, *40*, 4615–4627.
- (56) Neppalli, R.; Marega, C.; Marigo, A.; Bajgai, M. P.; Kim, H. Y.; Causin, V. Improvement of tensile properties and tuning of the biodegradation behavior of polycaprolactone by addition of electrospun fiber. *Polymer* **2011**, *52*, 4054–4060.
- (57) Kawai, T.; Rahman, N.; Matsuba, G.; Nishida, K.; Kanaya, T.; Nakano, M.; Okamoto, H.; Kawada, J.; Usuki, A.; Honma, N.; et al. Crystallization and Melting Behavior of Poly(L-lactic Acid). *Macromolecules* **2007**, *40*, 9463–9469.
- (58) Ashcraft, C. R.; Boyd, R. H. A Dielectric Study of Molecular Relaxation in Oxidized and Chlorinated Polyethylenes. *J. Polym. Sci. Polym. Phys. Ed.* **1976**, *14*, 2153–2193.

(59) Spiess, H. W. Interplay of Structure and Dynamics in Macromolecular and Supramolecular Systems. *Macromolecules* **2010**, *43*, 5479–5491.

(60) Hu, W.; Cai, T. Regime Transitions of Polymer Crystal Growth Rates: Molecular Simulations and Interpretation beyond Lauritzen–Hoffman Model. *Macromolecules* **2008**, *41*, 2049–2061.

(61) Hong, Y.; Miyoshi, T. Elucidation of the Chain-Folding Structure of a Semicrystalline Polymer in Single Crystals by Solid-State NMR. *ACS Macro Lett.* **2014**, *3*, 556–559.

(62) Hong, Y.; Miyoshi, T. Chain-Folding Structure of a Semicrystalline Polymer in Bulk Crystals Determined by ^{13}C – ^{13}C Double Quantum NMR. *ACS Macro Lett.* **2013**, *2*, 501–505.